Size Fractionation of Two-Dimensional Sub-Nanometer Thin Manganese Dioxide Crystals towards Superior Urea Electrocatalytic Conversion

Sheng Chen, Jingjing Duan, Anthony Vasileff, and Shi Zhang Qiao*

Abstract: *A universal technique has been proposed to sort two-dimensional (2D) sub-nanometer thin crystals (manganese dioxide MnO_2 and molybdenum disulfide MoS_2) according to their lateral dimensions. This technique is based on tuning the zeta potential of their aqueous dispersions which induces the selective sedimentation of large-sized 2D crystals and leaves the small-sized counterparts in suspension. The electrocatalytic properties of as-obtained 2D ultrathin crystals are strongly dependent on their lateral size. As a proof-of-concept study, the small-sized MnO_2 nanocrystals were tested as the electrocatalysts for the urea-oxidation reaction (UOR), which showed outstanding performance in both half reaction and full electrolytic cell. A mechanism study reveals the enhanced performance is associated with the remarkable structural properties of MnO_2 including ultrathin (ca. 0.95 nm), laterally small-sized (50–200 nm), and highly exposed active centers.*

Two-dimensional (2D) crystals such as transition-metal oxides and dichalcogenides are the leading successors to graphene with diverse properties and applications.[1] Like graphene, the properties of 2D nanocrystals are sensitive to structural features including, for example, thickness, lateral size, crystal planes, and defects.[2] Lateral size is particularly important and is correlated to the advanced properties of 2D nanocrystals.[2a] Typical examples include 2D manganese dioxide (MnO_2) and molybdenum disulfide (MoS_2), where the small-sized nanocrystals with more exposed edge sites favor electrocatalytic applications compared to their large-sized counterparts.[3] Generally, the small-sized 2D nanocrystals are useful for applications such as: catalysis, biosensing, and drug delivery,[4] while large-sized nanocrystals (> 500 nm) can restack themselves to form three-dimensional (3D) networks useful for energy storage.[5] Therefore, it is highly critical to control the lateral sizes of 2D crystals towards specific applications.

The direct synthesis of 2D nanocrystals can be achieved through either bottom-up (chemical synthesis,[6] template synthesis[7] and chemical vapour deposition[1b]) or top-down (liquid exfoliation[1a] and chemical swell[8]) methods. However, it is challenging to directly produce 2D nanocrystals with uniform lateral size. Inspired by graphene chemistry,[4a] post-synthetic procedures, such as centrifugation strategy, have recently been proposed to separate 2D nanocrystals with different lateral sizes.[2a] This strategy, however, limits scalable production because of the small volumes of centrifuge tubes, high centrifuging rate and usage of specialized equipment. Consequently, convenient and scalable techniques for the size fractionation of 2D nanocrystals remain to be exploited.

Urea electrolysis ($CO(NH_2)_2 + H_2O \rightarrow N_2 + 3H_2 + CO_2$) is a widely used technique for purifying urea-rich wastewater, while at the same time, producing hydrogen.[9] The primary step of urea electrolysis is the anodic urea-oxidation reaction (denoted as UOR; $CO(NH_2)_2 + 6OH^- \rightarrow N_2 + 5H_2O + CO_2 + 6e^-$), which has intrinsically sluggish kinetics owing to a $6e^-$ transfer process and complicated gas evolution steps (N_2 and CO_2).[9,10] Therefore, UOR usually requires noble metal-based catalysts such as platinum/carbon (Pt/C)[9] and rhodium.[10c] However, their scarcity and high price hinder the commercialization of the technique.

Recently, enormous efforts have been focused on developing low-cost alternatives to noble-metal catalysts such as: NiO nanosheets,[10f] Ni(OH)$_2$ nanotubes,[10a] and NiMoO$_4$ nanosheet arrays.[10b] There are few examples in the literature applying 2D ultrathin nanocrystals for UOR (i.e. Ni(OH)$_2$ nanolayers with a size distribution ranging from tens of nanometers to several micrometers[10d]), yet their catalytic activity underperforms relative to the noble-metal benchmark (Pt/C). It is practically necessary and economically desirable to develop alternative UOR catalysts with high activity but low price compared to Pt/C.

In this study, we report a simple post-synthetic procedure to produce 2D ultrathin nanocrystals with homogeneous lateral size. The key step of this procedure is to tune the zeta potential of their aqueous dispersions. The resultant materials were found to have excellent structural properties. The small-sized MnO_2 nanocrystals (denoted S-MnO_2) demonstrated a superior catalytic performance with high activity (2.2 times greater current density than the Pt/C benchmark), favorable kinetics, and strong durability. On the other hand, the large-sized MnO_2 nanocrystals (500 nm to several micrometers; denoted L-MnO_2) have been filtrated to form three-dimensional (3D) flexible papers for other applications. Further, this new procedure has been extended to the size fractionation of other nanostructures including 2D MoS_2 crystals and one-dimensional (1D) polyaniline nanorods.

As a proof-of-concept study, MnO_2 ultrathin nanocrystals were prepared through the redox reaction between potassium permanganate (KMnO$_4$) and sodium dodecyl sulphate (SDS). The lateral size of the original MnO_2 nanolayers ranged from tens of nanometers to several micrometers, as indicated by

[*] Dr. S. Chen, Dr. J. J. Duan, A. Vasileff, Prof. S. Z. Qiao
School of Chemical Engineering, The University of Adelaide
Adelaide, SA 5005 (Australia)
E-mail: s.qiao@adelaide.edu.au

Supporting information and the ORCID identification number(s) for the author(s) of this article can be found under http://dx.doi.org/10.1002/anie.201600387.

transmission electron microscopy (TEM; see Figure S1 in the Supporting Information). Fourier transform infrared spectroscopy (FT-IR; Figure S2) reveals that these nanolayers have highly hydrated structures because of the adsorption of water molecules (through covalent, hydrogen or hydration bonding) at both the basal planes and edge sites. Therefore, the MnO_2 nanolayers can be dispersed in water to form a stable colloidal dispersion. The zeta potential of the original MnO_2 dispersion was -39 mV (Figure S3), indicating that these nanolayers are negatively charged through the deprotonation of adsorbed water (H$-$O$-$H) into OH$^-$. Interestingly, after the zeta potential of the MnO_2 dispersion was tuned by adding hydrochloric acid (HCl), precipitation of MnO_2 nanolayers occurred after the dispersion was left still for 6 h (please see Experimental Section in the Supporting Information). The suspension and sediment were collected and characterized as S-MnO_2 and L-MnO_2, respectively.

To study the sedimentation process, the zeta potential of S- and L-MnO_2 was recorded as a function of the amount of added HCl (Figure 1 A). Without HCl, the zeta potentials of S- and L-MnO_2 are -35 and -30 mV, respectively, suggesting that the MnO_2 nanolayers are negatively charged in aqueous

media. The zeta potentials of both MnO_2 samples increased with the addition of HCl, leading to the reduced dispersibility of MnO_2 nanolayers in water.[11] In particular, the addition of 60 μL of 1M HCl to 5 mL of 1 mg mL^{-1} MnO_2 dispersion resulted in the largest zeta potential difference between S- and L-MnO_2 (-25 vs. -15 mV). Following this, precipitation of L-MnO_2 occurred after being left still for 6 h (Figure 1 B and its inset). It is also noted that excessive amounts of HCl (for example 100 μL; Figure S4) quickly precipitated both S- and L-MnO_2.

TEM reveals both S- and L-MnO_2 samples have ultrathin and almost transparent lamellar structures with graphene-like wrinkles and folds on the surfaces (Figure 1 C,D). The lateral size of S-MnO_2 is distributed between 50 to 200 nm, while L-MnO_2 is 500 nm to several micrometers. Additionally, atomic force microscopy (AFM) displays the roughly planar surface for a single S-MnO_2 nanolayer with a lateral dimension of about 170 nm (Figure 1 E). The height profile along the green line of the AFM image (Figure 1 E) reveals a thickness of about 0.95 nm, which agrees well with the thickness expected for a single-layer MnO_6 unit in MnO_2.[6] Both TEM (Figure 1 F) and scanning electron microscopy (SEM; Figure S5) elemental mappings show that Mn and O are homogeneously distributed throughout the nanolayer.

X-ray diffraction (XRD; Figure 2 A) profiles of both S- and L-MnO_2 exhibit four main characteristic peaks in line with those of a δ-MnO_2 phase (JCPDS number 18-0802). This result is complimented by Raman spectra (Figure 2 B), where the Raman band around 635 cm^{-1} for both S- and L-MnO_2 corresponds to the symmetric stretching Mn$-$O vibration of MnO_6 groups.[12] Additionally, X-ray photoelectron spectra (XPS; Figures 2 C,D and S6) reveal that both samples are mainly composed of MnO_2 with seldom Mn_2O_3 or $KMnO_4$ impurities.[13] Moreover, the nitrogen adsorption isotherm shown in Figure 2 E resembles type IV with a narrow hysteresis loop and the Brunauer–Emmett–Teller (BET) surface area of S-MnO_2 exceeds that of L-MnO_2 (111 vs. 75 m^{2}g^{-1}). Thermogravimetric analysis (TGA; Figure 2 F) plots of both samples indicate a continuous mass loss from 100 to 500°C, caused by the removal of structural water (ca. 200°C) and phase transition from MnO_2 to Mn_2O_3 (ca. 500°C; Figure 1 H).[13] A greater mass loss for S-MnO_2 from 100°C to 500°C than that of L-MnO_2 is due to the more exposed edges and thus more absorbed water.

S-MnO_2 is prepared as an electrocatalyst and studied for UOR (Figures 3 A and S7). The working electrode is prepared by incorporating S-MnO_2 nanolayers into three-dimensional (3D) graphene–nickel foam (NF) hybrid films (denoted as NF-G-Mn), where NF is the substrate framework and graphene is the conductive agent (inset of Figures 3 A and S8). S-MnO_2 inside NF-G-Mn has an average mass loading of 1.5 mg cm^{-2} and other comparison samples such as L-MnO_2, Pt/C, bulk MnO_2, 2D S-MnO_2 (where graphene–MnO_2 composite from NF-G-Mn is deposited onto 2D glassy carbon) and G-NF (graphene deposited on nickel foam) are all prepared with similar loadings. In a typical linear sweep voltammogram (LSV) plot, the anodic current of all samples simultaneously increases as the potential becomes more positive, which is commonly observed for UOR catalysis in
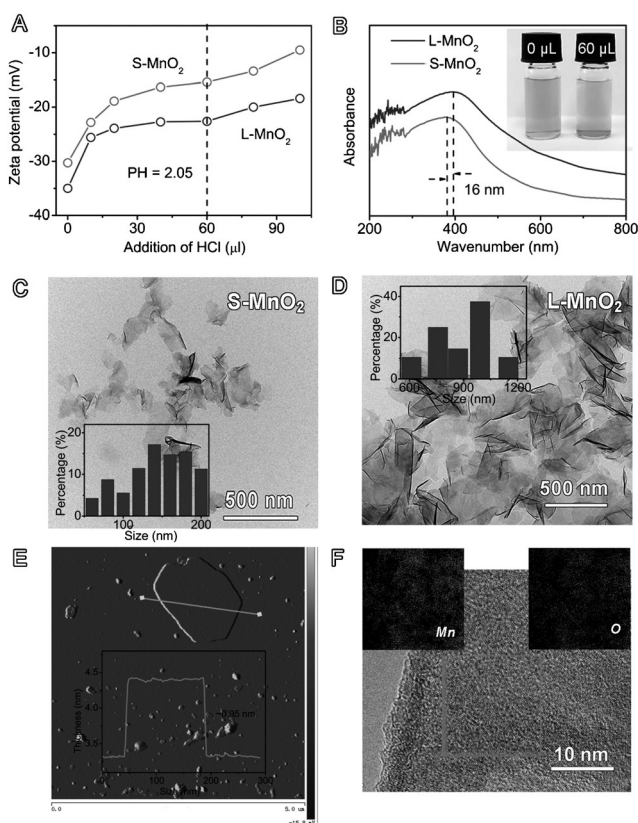

Figure 1. A) Zeta potential of S- and L-MnO_2 nanolayer aqueous dispersions (1 mg mL^{-1}, 5 mL) as a function of the added amount of 1M of HCl solution (0, 20, 40, 60, 80, 100 μL). B) UV/Vis spectra of S- and L-MnO_2 nanolayers. The inset of (B) shows the optical images of original MnO_2 nanolayers with and without adding HCl (1M, 60 μL) after left still over for 6 h. C,D) TEM images of S- and L-MnO_2 nanolayers with the size distribution histograms. E) AFM image of a S-MnO_2 nanolayer. F) HRTEM image and corresponding element mapping of a S-MnO_2 nanolayer.
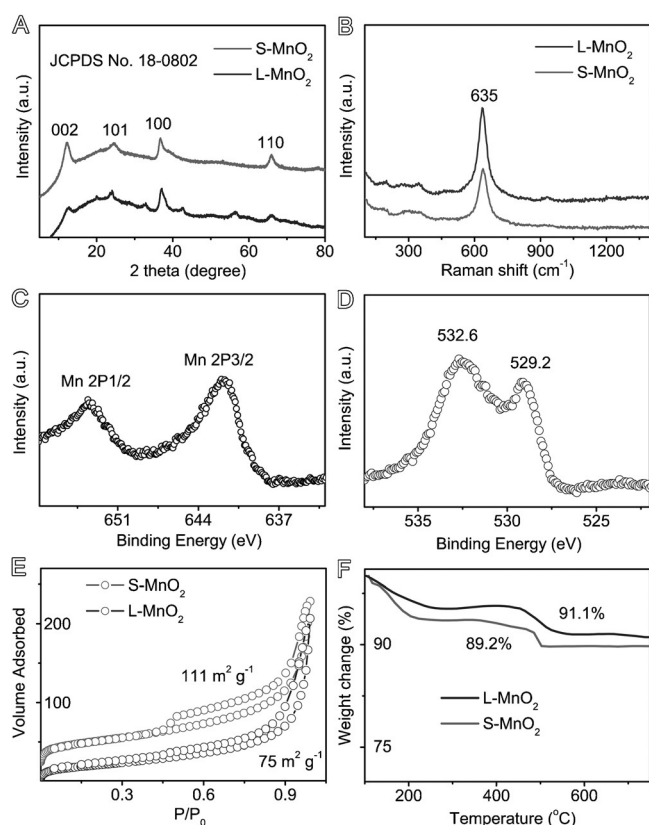
Figure 2. The structural analyses of MnO_2 nanolayers. A) XRD patterns of S- and L-MnO_2 nanolayers. B) Raman spectra of S- and L-MnO_2 nanolayers. C,D) XPS Mn and O spectra of S-MnO_2 nanolayers. E) Nitrogen adsorption–desorption isotherm (expressed in cm^3 STP g^{-1}) of S- and L-MnO_2 nanolayers. F) TGA plots of S- and L-MnO_2 nanolayers.
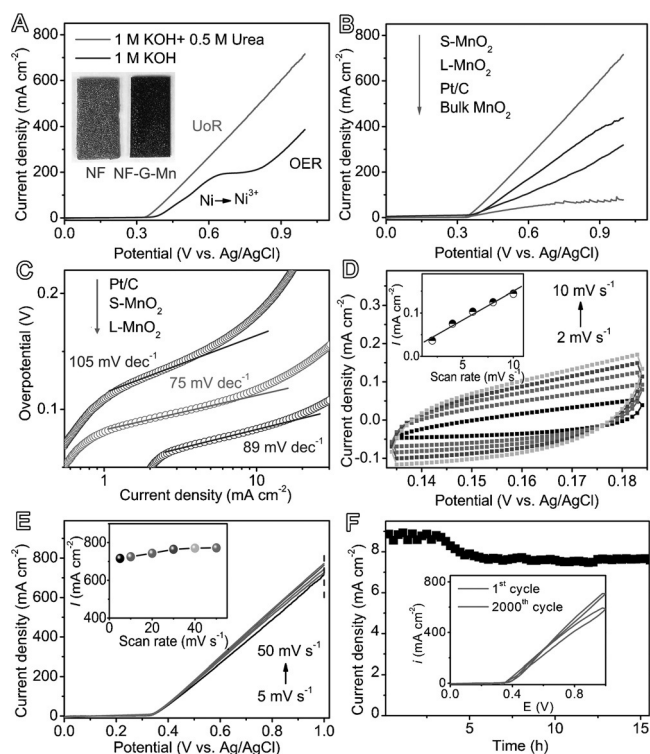

Figure 3. UOR catalytic properties of MnO_2 electrode. A) Linear sweep voltammetry (LSV) plots of S-MnO_2-G-NF in 1 M KOH electrolyte with and without 0.5 M urea. The inset of (A) shows optical images of a NF-G-Mn electrode and NF substrate. B) LSV plots of NF-G-Mn compared with L-MnO_2, Pt/C, and bulk MnO_2. C) Tafel plots of NF-G-Mn compared with L-MnO_2 and Pt/C. D) CVs of NF-G-Mn measured at different scan rates from 2 to 10 mV s^{-1} in the potential region of 0.134–0.184 (vs. Ag/AgCl). The inset of (D) shows the current density at 0.174 (vs. Ag/AgCl) plotted versus scan rate. E) LSV plots for NF-G-Mn at different scan rates. The inset in (E) shows the corresponding data re-plotted as the current density (at 1.0 V vs. Ag/AgCl) at different scan rates. F) Chronoamperometric response of NF-G-Mn in 0.5 M urea + 1 M KOH electrolyte at 0.35 V (vs. Ag/AgCl) for 16 h. The inset in (F) shows CVs at 10 mV s^{-1} before and after operation for 2000 cycles.

alkaline media (Figure 3 A,B).[9–10] Large amount of gas products (N_2 and CO_2) are generated with elevating potentials (Video S1), indicating UOR has successfully occurred at the NF-G-Mn electrode. Note that the UOR process at NF-G-Mn cannot take place without urea (i.e. only oxygen evolution occurs,[14] Figure 3 A) and/or KOH (Figure S9).

NF-G-Mn demonstrates excellent UOR performance with a high catalytic activity and favorable reaction kinetics (Figures 3 B, S10, and S11). Specifically, NF-G-Mn has a smaller overpotential of 1.33 V (vs. reversible hydrogen electrode, RHE, at the current density of 10 mA cm^{-2}) than other samples such as L-MnO_2 (1.37 V), Pt/C (1.48 V), bulk MnO_2 (1. 55 V), 2D S-MnO_2 (1.68 V), nickel foam (1.56 V), and G-NF (1.58 V). The UOR kinetics were also studied by comparing their Tafel plots (Figure 3 C). A Tafel slope of 75 mV dec^{-1} for NF-G-Mn is marginally smaller than that of L-MnO_2 (89 mV dec^{-1}) and much lower than that of Pt/C (105 mV dec^{-1}), suggesting its favorable catalytic kinetics for UOR. Remarkably, the catalytic current density of NF-G-Mn is much greater than that of Pt/C (716 vs. 318 mA cm^{-2} at 2.02 V vs. RHE). The high UOR activity of NF-G-Mn is further verified by its roughness factor (R_f of 231; Figures 3 D and S12)[15] and its excellent capability (< 10 % current change from 5 to 50 mV s^{-1}; Figures 3 E and S13 A). By

comparison with other catalysts in the literature (Table S1), NF-G-Mn is among the most active electrocatalysts for UOR.

High stability towards UOR is also important for long-term catalytic performance. The electrodes show excellent catalytic stability with an activity decay of less than 10 % after operation for 16 h (Figure 3 F), in contrast to a sharp activity loss of 2D S-MnO_2 (retaining 63.4 % after 400 s; Figure S14). The slight decrease of performance around 5 h (ca. 6 %) is due to the reorganization of active species within electrodes as well as the loss of active species during the gas-evolution process.[10a,b] The strong stability of NF-G-Mn is also verified by a continuous potential cycling test (2000 cycles) which reveals only slight change in current density at 1 V versus Ag/AgCl (< 10 %; inset of Figure 3 F). Further, the overall urea electrolysis was established by coupling the NF-G-Mn anode with a cobalt phosphide–nickel foam cathode (Figures 4 A and S15 and Video S2), which quickly generated gas bubbles at both anode (CO_2 and N_2 through UOR) and cathode (H_2 through HER). The CoP_x-NF cathode was prepared by
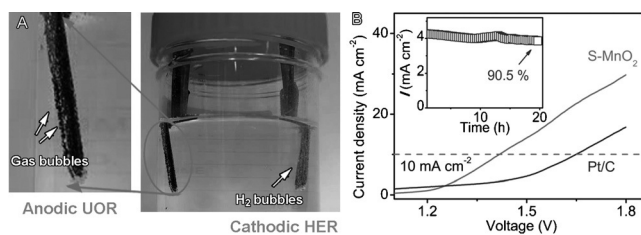
Figure 4. Overall urea electrolysis based on S-MnO electrode. A) The optical image of urea electrocatalysis in 0.5 M urea + 1 M KOH electrolyte at the voltage of 1.8 V using NF-G-Mn as an anode and CoPx-NF as a cathode. B) LSV plots of urea electrolysis at S-MnO$_2$ based NF-G-Mn/CoPx-NF and Pt/C-Pt/C cells. The inset of (B) shows the chronoamperometric response of NF-G-Mn/CoPx-NF cell working for urea electrolysis at a voltage of 1.4 V for 20 h.

a simple electrodeposition method (see the Experimental Section in the Supporting Information), and its structure and morphology were characterized by SEM, EDS, and elemental mapping (Figure S15 A–E). CoP$_x$-NF has been used as the cathodic electrode becuause of its low price along with its high catalytic activity towards HER with an overpotential comparable to the Pt/C benchmark (−1.01 V vs. −0.98 V vs. Ag/AgCl; Figure S15 F). As expected, the full electrocatalytic system showed excellent activity by delivering a current density of 10 mA cm^{-2} at 1.41 V (vs. 1.68 V for Pt/C, and 1.72 V for Pt/C-IrO$_2$ pair electrodes), and worked smoothly for at least 20 h (Figures 4 B and S16). These outstanding features indicate that NF-G-Mn is an excellent catalyst for UOR.

Studying the mechanism of UOR with NF-G-Mn electrodes indicates that S-MnO$_2$ provides the main catalytic centres. Without S-MnO$_2$, NF or NF-G alone show negligible catalytic activity in comparison to NF-G-Mn (Figure S11). On the other hand, the enhanced performance of NF-G-Mn is associated with its remarkable structural properties. First, S-MnO$_2$ can provide rich active centers because of the extremely exposed edges and planar surfaces. Therefore, S-MnO$_2$ based electrodes exhibit a higher roughness factor than its L-MnO$_2$ and bulk MnO$_2$ counterparts (231 vs. 193 and 104, Figures 3 D and S12) and consequently, a higher catalytic activity (Figure 3 B). Second, the incorporation of S-MnO$_2$ into a graphene-nickel foam substrate forms a 3D-architectured electrode with rich porosity, which is revealed by SEM (Figure S8) and nitrogen adsorption isotherm (Figure 2 E). The highly porous structure can facilitate mass transport and infiltration of electrolytes, thereby enhancing the UOR kinetics as indicated by a small Tafel slope (Figure 3 C) and excellent rate capability (Figures 3 E and S13). Further, the 3D NF-G-Mn electrode exhibits excellent electrochemical stability toward UOR, which is differnt from its 2D S-MnO counterpart with rapid activity loss (Figure S14). As seen in Figure S8, S-MnO$_2$ nanolayers have been fully accommodated in the graphene sheets of the NF-G-Mn electrode, where their volume change during the catalytic process can be effectively buffered by adjacent graphene sheets with excellent mechanical properties, thus affording high electrode durability.

Supplementary experiments were conducted to demonstrate the benefits and universal application of this size fractionation technique. Firstly, L-MnO$_2$ can form 3D flexible films using a simple vacuum-assisted filtration procedure. The film has an average planar size of several centimeters and thickness of around 16 micrometers, as confirmed by the optical image (Figure S17 A) and SEM images (Figure S17 B,C). These 3D macroscopic films made entirely of 2D MnO$_2$ nanolayers can find potential applications in supercapacitors.[9] Secondly, this technique has been extended to process other 2D and 1D nanostructured materials. 2D MoS$_2$ nanolayers prepared from a top–down exfoliation procedure[16] can also disperse homogeneously in water with a zeta potential of −21.1 mV (Figure S18 A). HCl was used to adjust the zeta potential of these aqueous dispersions which induced the selective precipitation of MoS$_2$ for size fractionation (Figure S18 B). 1D polyaniline (PANI) nanorods, synthesized according to the previous report,[17] have a typical diameter of 120 nm and length ranging from several hundred nanometers to several micrometers. The PANI was positively charged in water with a zeta potential of 43 mV (Figure S19 A). By adjusting the zeta potential using alkali, the PANI was also selectively precipitated by length (Figure S19 B).

In conclusion, a universal technique has been demonstrated for the size fractionation of 2D nanolayer materials by adjusting the zeta potential of their aqueous dispersions. Small but relatively uniform MnO$_2$ nanolayers favor electrocatalytic applications such as the UOR and exhibit excellent performance with high activity, favorable kinetics and strong catalyst durability. Further, an overall urea electrolytic cell was built using MnO$_2$ nanolayer hybrid electrodes as the cathode. This electrolytic cell demonstrated excellent electrochemical performance towards the purification of urea-rich wastewater and simultaneous hydrogen generation. This work may shed light on processing a wide range of other materials for energy storage and conversion such as water splitting, metal–air batteries, fuel cells, and carbon dioxide reduction.

How to cite: *Angew. Chem. Int. Ed.* **2016**, *55*, 3804–3808
Angew. Chem. **2016**, *128*, 3868–3872

[1] a) J. N. Coleman, et al., *Science* **2011**, *331*, 568–571; b) Y. Gong, et al., *Nat. Mater.* **2014**, *13*, 1135–1142.

[2] a) C. Backes, et al., *Nat. Commun.* **2014**, *5*, 4576; b) J. Kang, J. W. Seo, D. Alducin, A. Ponce, M. J. Yacaman, M. C. Hersam, *Nat. Commun.* **2014**, *5*, 5478.

[3] a) J. Xie, H. Zhang, S. Li, R. Wang, X. P. Sun, M. Zhou, J. Zhou, X. W. Lou, Y. Xie, *Adv. Mater.* **2013**, *25*, 5807–5813; b) H. I.

Karunadasa, E. Montalvo, Y. Sun, M. Majda, J. R. Long, C. J. Chang, *Science* **2012**, *335*, 698 – 702.

[4] a) X. Wang, H. Bai, G. Q. Shi, *J. Am. Chem. Soc.* **2011**, *133*, 6338 – 6342; b) T. Liu, C. Wang, X. Gu, H. Gong, L. Cheng, X. Shi, L. Feng, B. Sun, Z. F. Liu, *Adv. Mater.* **2014**, *26*, 3433 – 3440; c) F. Song, X. Hu, *J. Am. Chem. Soc.* **2014**, *136*, 16481 – 16484; d) M. Zhang, et al., *J. Am. Chem. Soc.* **2014**, *136*, 7241 – 7244.

[5] a) M. Acerce, D. Voiry, M. Chhowalla, *Nat. Nanotechnol.* **2015**, *10*, 313 – 318; b) M. Ghidiu, M. R. Lukatskaya, M. Q. Zhao, Y. Gogotsi, M. W. Barsoum, *Nature* **2014**, *516*, 78 – 81.

[6] a) Z. Liu, K. Xu, H. Sun, S. Yin, *Small* **2015**, *11*, 2182 – 2191; b) H. Wang, J. Zhang, X. Hang, X. Zhang, J. Xie, B. Pan, Y. Xie, *Angew. Chem. Int. Ed.* **2015**, *54*, 1195 – 1199; *Angew. Chem.* **2015**, *127*, 1211 – 1215.

[7] J. S. Son, et al., *Angew. Chem. Int. Ed.* **2009**, *48*, 6861 – 6864; *Angew. Chem.* **2009**, *121*, 6993 – 6996.

[8] F. Song, X. L. Hu, *Nat. Commun.* **2014**, *5*, 4477.

[9] B. K. Boggs, R. L. King, G. G. Botte, *Chem. Commun.* **2009**, 4859 – 4861.

[10] a) R.-Y. Ji, D.-S. Chan, J.-J. Jow, M.-S. Wu, *Electrochem. Commun.* **2013**, *29*, 21 – 24; b) Y. Liang, Q. Liu, A. M. Asiri, X. P. Sun, *Electrochim. Acta* **2015**, *153*, 456 – 460; c) A. T. Miller, B. L. Hassler, G. G. Botte, *J. Appl. Electrochem.* **2012**, *42*, 925 –

934; d) D. Wang, W. Yan, G. G. Botte, *Electrochem. Commun.* **2011**, *13*, 1135 – 1138; e) D. Wang, W. Yan, S. H. Vijapur, G. G. Botte, *Electrochim. Acta* **2013**, *89*, 732 – 736; f) M.-S. Wu, G.-W. Lin, R.-S. Yang, *J. Power Sources* **2014**, *272*, 711 – 718.

[11] a) J. Chen, Y. Li, L. Huang, N. Jia, C. Li, G. Q. Shi, *Adv. Mater.* **2015**, *27*, 3654 – 3660; b) D. Li, M. B. Müller, S. Gilje, R. B. Kaner, G. G. Wallace, *Nat. Nanotechnol.* **2008**, *3*, 101 – 105.

[12] C. Julien, *Solid State Ionics* **2003**, *159*, 345 – 356.

[13] S. Chen, J. J. Duan, W. Han, S. Z. Qiao, *Chem. Commun.* **2014**, *50*, 207 – 209.

[14] R. Subbaraman, D. Tripkovic, K. C. Chang, D. Strmcnik, A. P. Paulikas, P. Hirunsit, M. Chan, J. Greeley, V. Stamenkovic, N. M. Markovic, *Nat. Mater.* **2012**, *11*, 550 – 557.

[15] Y. Li, P. Hasin, Y. Wu, *Adv. Mater.* **2010**, *22*, 1926 – 1929.

[16] K.-G. Zhou, N.-N. Mao, H.-X. Wang, Y. Peng, H.-L. Zhang, *Angew. Chem. Int. Ed.* **2011**, *50*, 10839 – 10842; *Angew. Chem.* **2011**, *123*, 11031 – 11034.

[17] D. Li, R. B. Kaner, *J. Am. Chem. Soc.* **2006**, *128*, 968 – 975.